

Mapping dynamical ejecta and disk masses from numerical relativity simulations of neutron star mergers

Vsevolod Nedora¹, Federico Schianchi^{2,1}, Sebastiano Bernuzzi¹, David Radice^{3,4,5}, Boris Daszuta¹, Andrea Endrizzi¹, Albino Perego^{6,7}, Aviral Prakash^{3,4}, and Francesco Zappa¹

¹*Theoretisch-Physikalisches Institut, Friedrich-Schiller-Universität Jena, 07743, Jena, Germany*

²*Institut für Physik und Astronomie, Universität Potsdam,*

Haus 28, Karl-Liebknecht-Str. 24/25, 14476, Potsdam, Germany

³*Institute for Gravitation & the Cosmos, The Pennsylvania State University, University Park, PA 16802, USA*

⁴*Department of Physics, The Pennsylvania State University, University Park, PA 16802, USA*

⁵*Department of Astronomy & Astrophysics, The Pennsylvania State University, University Park, PA 16802, USA*

⁶*Dipartimento di Fisica, Università di Trento, Via Sommarive 14, 38123 Trento, Italy and*

⁷*INFN-TIFPA, Trento Institute for Fundamental Physics and Applications, via Sommarive 14, I-38123 Trento, Italy*

(Dated: November 24, 2020)

We present fitting formulae for the dynamical ejecta properties and remnant disk masses from a large sample of numerical relativity simulations. The considered data include some of the latest simulations with microphysical nuclear equations of state (EOS) and neutrino transport as well as other results with polytropic EOS available in the literature. Our analysis indicates that the broad features of the dynamical ejecta and disk properties can be captured by fitting expressions, that depends on mass ratio and reduced tidal parameter. The comparative analysis of literature data shows that microphysics and neutrino absorption have a significant impact on the dynamical ejecta properties. Microphysical nuclear equations of state leads to average velocities smaller than polytropic EOS, while including neutrino absorption results in larger average ejecta masses and electron fractions. Hence, microphysics and neutrino transport are necessary to obtain quantitative models of the ejecta in terms of the binary parameters.

I. INTRODUCTION

The UV/optical/NIR transient AT2017gfo [1–14], counterpart of the gravitational-wave signal GW170817 [15–18], is explained as the kilonova signal from the radioactive decay of r -process elements synthesized in the mass ejected during binary neutron star mergers [10, 19–32]. Minimal models of the kilonova AT2017gfo require at least two ejecta components to account for the observed light curves: a lanthanide-poor (for the blue signal) and a lanthanide-rich (for the red signal) one [10, 28–32]. These components are often identified as the dynamical ejecta and the wind ejecta from the remnant disk, although simulations clearly indicate that this interpretation is not complete. *e.g.*, [33, 34]

Mass ejection in mergers can be triggered by different mechanisms acting on different timescales (see [35–38] for reviews on various aspects of the problem). Simulations robustly identify dynamical ejecta, of mass $M_{\text{ej}} \sim \mathcal{O}(10^{-4} - 10^{-2}) M_{\odot}$ launched during merger at average velocities $\langle v_{\infty} \rangle \sim 0.1 - 0.3 c$, *e.g.*, [23, 24, 39–45], and (for many fiducial postmerger configurations) more massive but slower winds launched on secular timescales from the remnant disk [33, 46–58]. The most accurate approach to compute the dynamical ejecta and the remnant evolution is to employ ab-initio 3+1 simulations in numerical relativity, *e.g.*, [39, 41–45, 59–68]. The increasing amount of data (both in terms of simulated binaries, physics input and numerical resolutions) allows us to explore the dependencies of ejecta and remnant properties on the binary parameters. Fitting formulae of numerical relativity data for the dynamical ejecta and remnant disk

properties from binary neutron star mergers have been previously presented in [64, 69, 70]. The interest in these formulae is at least twofold. On the one hand, they can be used to identify the main parametric dependencies of the ejecta mechanisms; on the other hand, they can be employed to constrain the source parameters from kilonova observations, *e.g.*, [31, 71–73]. Additionally, they are key to predict the amount and the properties of the ejecta that enter chemical evolution models, *e.g.*, [74].

Here we employ an extended set of data presented in previous works that includes also recent simulations with approximate neutrino transport and large mass ratios [34, 65, 68, 75]. We re-calibrate the fit models proposed in the literature with this extended dataset. Additionally we test simple polynomials as fitting models for the ejecta mass, velocity, and electron fraction. Moreover we employ a formula for the electron fraction of the dynamical ejecta inspired by a widely used model for the velocity [64, 69].

Throughout the paper we label the two NSs with subscripts A, B . The individual gravitational masses are indicated as M_A, M_B , the baryonic masses as M_{bA}, M_{bB} , the total mass as $M = M_A + M_B$, and the mass ratio $q = M_A/M_B \geq 1$. We define the quadrupolar tidal parameters as $\Lambda_i \equiv 2/3 C_i^{-5} k_i^{(2)}$ where $k_i^{(2)}$ is the dimensionless gravitoelectric Love number [78], $C_i \equiv GM_A/(c^2 R_A)$ the compactness parameter, and $i = A, B$. The reduced tidal parameter [79] is:

$$\tilde{\Lambda} = \frac{16 (M_A + 12M_B) M_A^4 \Lambda_A}{13 M^5} + (A \leftrightarrow B). \quad (1)$$

We use CGS units except for masses and velocities, given

TABLE I. Datasets with the dynamical ejecta data and disk masses employed in this work. The available data is shown in the columns starting from the fourth, that contain: gravitational mass of the binary, baryonic mass of the binary, reduced tidal parameter, ejecta mass, ejecta velocity, ejecta electron fraction, disk/torus mass. EOS are either microphysical or piecewise polytropic (PWP). Neutrino schemes are: leakage, leakage + M0 or M1 for free streaming neutrinos, or M1. The compiled data are available online at [76].

Ref.	EOS	Neutrinos	M	M_b	$\tilde{\Lambda}$	M_{ej}	v_{ej}	Y_e	M_{disk}	Dataset
[65]	Micro	Leak+M0	✓	✓	✓	✓	✓	✓	✓	M0RefSet & M0/M1Set
[75]	Micro	Leak+M0	✓	✓	✓	✓	✓	✓	✓	M0RefSet & M0/M1Set
[68]	Micro	Leak+M0	✓	✓	✓	✓	✓	✓	✓	M0RefSet & M0/M1Set
[34]	Micro	Leak+M0	✓	✓	✓	✓	✓	✓	✓	M0RefSet & M0/M1Set
[45]	Micro	M1	✓	✓	✓	✓	✓	✓	✗	M0/M1Set
[42]	Micro	Leak+M1	✓	✗	✗	✓	✗	✓	✗	M0/M1Set
[44]	Micro	Leak+M1	✓	✗	✗	✓	✓	✓	✓	M0/M1Set
[64](M0)	Micro	Leak+M0	✓	✓	✓	✓	✓	✓	✓	M0/M1Set
[63]	Micro	Leak	✓	✓	✗	✓	✓	✗	✗	LeakSet
[64](LK)	Micro	Leak	✓	✓	✓	✓	✓	✓	✓	LeakSet
[66]	PWP	-	✓	✓	✓	✓	✗	✗	✓	NoNusSet
[77]	PWP	-	✓	✓	✓	✓	✓	✗	✓	NoNusSet
[77]	PWP	-	✓	✓	✓	✓	✓	✗	✓	NoNusSet
[59]	PWP	-	✓	✗	✗	✓	✓	✗	✗	NoNusSet
[40]	Micro	-	✓	✗	✗	✓	✓	✗	✗	NoNusSet

in units of M_\odot and c , respectively.

II. DATA & METHOD

The datasets used in this paper are summarized in Tab. I. We group them with respect to the employed neutrino treatment:

- **M0/M1Set** is a set of runs with neutrino emission and absorption, and microphysical EOS, including the 8 models with leakage+M0 of [64] (denoted as M0), the models of [34, 65, 68, 75], and the models of [42, 44, 45] in which a leakage+M1 scheme or a M1 gray scheme are employed for the neutrino transport. Models reported in these works span $q \in [1, 1.30]$, $\tilde{\Lambda} \in [340, 1437]$, $M_{tot} \in [2.52, 2.88]$, and $M_{chirp} \in [1.10, 1.25]$.
- **M0RefSet** is a subset of **M0/M1Set**. It consists of only the models presented in [34, 65, 68, 75]. The models of this set span $q \in [1, 1.82]$, $\tilde{\Lambda} \in [400, 850]$, $M_{tot} \in [2.73, 2.88]$ for a fixed chirp mass $M_{chirp} = 1.19$. This sample is homogeneous in terms of NR code, of computational and physical setups, and of chirp mass. Hence, we use it as a reference dataset.
- **LeakSet** is a set of runs with leakage scheme as neutrino treatment and microphysical EOS, including a subset of the runs contained in [64] (35 runs denoted as LK), and the set of models from [63]. The models in this dataset span $q \in [1, 1.31]$, $\tilde{\Lambda} \in [116, 1688]$, $M_{tot} \in [2.40, 3.42]$, and $M_{chirp} \in [1.04, 1.49]$.
- **NoNusSet** includes the piecewise-polytropic EOS runs of [40, 59, 60, 66, 77], in which temperature

effects are approximated by a gamma-law pressure contribution, while composition and weak effects are neglected. The models in this dataset span $q \in [1, 2.06]$, $\tilde{\Lambda} \in [50, 3196]$, $M_{tot} \in [2.4, 4.0]$, and $M_{chirp} \in [1.04, 1.74]$.

Overall, in aforementioned literature 324 models are available. For each distinct model, the reduced tidal parameter $\tilde{\Lambda}$ is computed by solving the TOV equations for the corresponding gravitational masses of the stars and EOS. However, for a subset of models with polytropic EOS of [80] and [66], the EOS data are not available and some binary parameters can not be computed.

Thus, out of 324, we have or compute the binary parameters for 271 models. For all of them the ejecta mass, M_{ej} , is available. For the models in [66] the ejecta velocity is not reported, thus only for 246 models the mass-averaged ejecta velocity, $\langle v_\infty \rangle$, is given. In addition to **NoNusSet** models, the average electron fraction of the ejecta is not provided also in [63]. Hence, there are 99 models for which the mass-averaged electron fraction of the dynamical ejecta, $\langle Y_e \rangle$, is available. Finally, for 76 models the root mean square (RMS) half opening angle of the outflow about the equatorial plane, $\langle \theta_{RMS} \rangle$, is available. The disk mass, M_{disk} , is provided for 119 models.

Since uncertainties estimates are not available for all datasets, we assign errors following Ref. [64]. For the dynamical ejecta mass we consider an uncertainty given by:

$$\Delta M_{ej} = 0.5 M_{ej} + 5 \times 10^{-5} M_\odot. \quad (2)$$

For the ejecta velocity and for the electron fraction we consider $\Delta v_{ej} = 0.02 c$ and $\Delta Y_e = 0.01$ as fiducial uncertainties, respectively. The latter value is justified

by the robust behavior of the average electron fraction in simulations where multiple resolutions are available ¹.

For the disk mass we assume [64]

$$\Delta M_{\text{disk}} = 0.5M_{\text{disk}} + (5 \times 10^{-4})M_{\odot}. \quad (3)$$

The analysis performed in this paper is based on the following procedure. We begin with a study of the overall properties of **M0RefSet**, then we add the models with microphysical EOS and neutrino heating and cooling of **M0/M1Set**, then we add models with only neutrino cooling of **LeakSet**, and finally we consider the total set of models by also including **NoNusSet**. We calibrate various fitting formulae using the least-square method, that minimizes the reduced χ^2 statistics (see below) for the ejecta quantities and residuals for the disk mass.

To compare different fitting formulae (for each ejecta property) we employ the reduced χ^2 statistics:

$$\chi_{\nu}^2 = \frac{\chi^2}{N-C} = \frac{1}{N-C} \sum_{i=1}^N \left(\frac{o_i - e_i}{o_i^{\text{err}}} \right)^2, \quad (4)$$

where N is the number of points in the dataset, C is the number of coefficients in the fitting model (thus $N-C$ defines the number of degrees of freedom), o_i are the dataset values and o_i^{err} their errors, e_i are the values predicted by the fitting model, and $o_i - e_i$ are the residuals. The model comparison thus states that the closer to 1 χ_{ν}^2 is, the better the model performs. In addition we compute the coefficient of determination, R^2 :

$$R^2 = 1 - \frac{\sum_{i=1}^N (o_i - e_i)^2}{\sum_{i=1}^N (o_i - \mu)^2}, \quad (5)$$

where μ is the mean value of $\{o_i\}_{i=1,N}$. Thus, the closer to one R^2 is, the better the fit performs.

III. DYNAMICAL EJECTA

The mechanism behind the production of dynamical ejecta as well as the details on the numerical relativity simulations of **M0RefSet** are discussed in *e.g.*, [34, 37, 38]. Here, we focus on overall properties of the mass ejecta in relation to other results in the literature, and provide approximate fitting formulae for the total ejecta mass, the mass-averaged velocity, the electron fraction and the rms half opening angle.

Figure 1 summarizes the total mass, the mass-averaged velocity and mass-averaged electron fraction (where

available) for the used datasets. Overall we note that the ejecta properties of the models of **M0RefSet** are compatible with those of **M0/M1Set**, as they include the same physics with respect to the EOS treatment and also include the effect of neutrino absorption. Notably, the very high mass-ratio, q , models of **M0RefSet**, discussed in [68], show slightly different properties, as their ejecta is of tidal origin only. Comparing the properties of **M0/M1Set** and **LeakSet** we observe that neutrino absorption leads, on average, to a larger ejecta mass, which is especially noticeable for the leakage subset of [64](LK). Additionally, neutrino absorption leads to a higher $\langle Y_e \rangle$ of the ejecta, while the average velocity, $\langle v_{\infty} \rangle$, appears to be independent of it.

In the following we discuss the fitting formulae for the different quantities.

A. Mass

The dynamical ejecta mass, averaged over all simulations in **M0RefSet**, is:

$$\overline{M_{\text{ej}}} = (3.51 \pm 2.57) \times 10^{-3} M_{\odot}, \quad (6)$$

where hereafter we report also the standard deviation computed over the relevant simulation sample. Adding the rest of **M0/M1Set** we obtain $(4.17 \pm 3.65) \times 10^{-3} M_{\odot}$. The increase is given largely by datasets that include the M1 neutrino scheme, [45] and [44]. However, adding models of **LeakSet**, we observe that the mean value decreases to $2.91 \times 10^{-3} M_{\odot}$, as models without neutrino absorption predict, on average, lower ejecta masses. Finally, adding models without neutrinos at all, some of which have polytropic EOS, results in an increase of the mean ejecta mass up to $5.56 \times 10^{-3} M_{\odot}$, as models with polytropes, in particular [77], give the largest M_{ej} among all the considered models.

We fit the data using second-order polynomials in one parameter ($\tilde{\Lambda}$), and in two parameters, $(q, \tilde{\Lambda})$, namely:

$$P_2^1(\tilde{\Lambda}) = b_0 + b_1 \tilde{\Lambda} + b_2 \tilde{\Lambda}^2, \quad (7)$$

$$P_2^2(q, \tilde{\Lambda}) = b_0 + b_1 q + b_2 \tilde{\Lambda} + b_3 q^2 + b_4 q \tilde{\Lambda} + b_5 \tilde{\Lambda}^2. \quad (8)$$

We also consider the model presented in [64, 69, 84]:

$$\left(\frac{M_{\text{ej}}}{10^{-3} M_{\odot}} \right)_{\text{fit}} = \left[\alpha \left(\frac{M_B}{M_A} \right)^{1/3} \left(\frac{1-2C_A}{C_A} \right) + \beta \left(\frac{M_B}{M_A} \right)^n + \gamma \left(1 - \frac{M_A}{M_{bA}} \right) \right] M_{bA} + (A \leftrightarrow B) + \delta, \quad (9)$$

and the model presented in [70]:

$$\left(\frac{M_{\text{ej}}}{10^{-3} M_{\odot}} \right)_{\text{fit}} = \left(\frac{\alpha}{C_A} + \beta \frac{M_B^n}{M_A^n} + \gamma C_A \right) M_A + (A \leftrightarrow B). \quad (10)$$

¹ We expect larger uncertainties due to the approximate nature of current neutrino treatments (see *e.g.* [81, 82]). However, due to the lack of extensive comparison studies, we consider only the numerical resolution error.

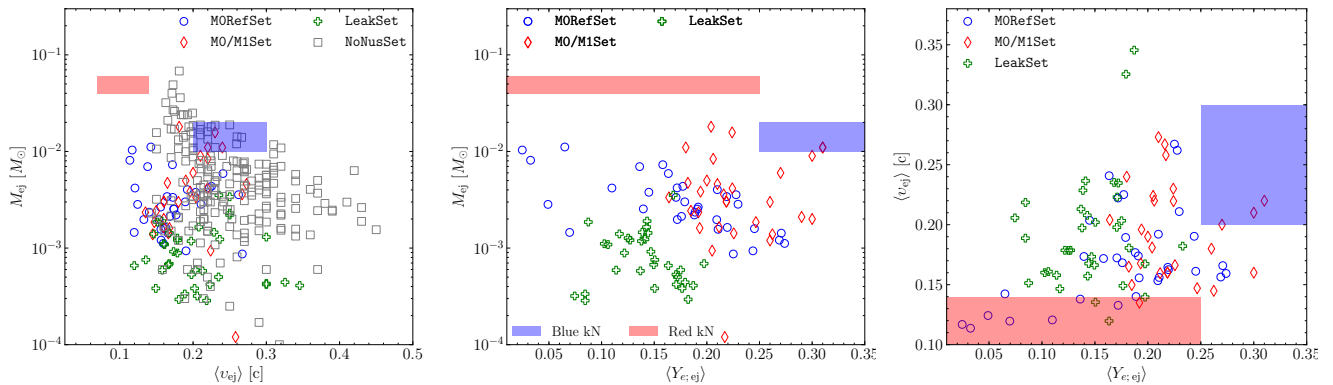


FIG. 1. Summary of dynamical ejecta properties used in this work. Blue circles represent models of **M0RefSet**, red diamonds stands for models from **M0/M1Set**, green crosses are models from **LeakSet** and gray squares stand for models from **NoNusSet**. We show for comparison the two-component fit to AT2017gfo as colored patches from [29, 83].

As in some cases the values of M_{ej} change by orders of magnitude for very close values of q and $\tilde{\Lambda}$, we calibrate the fitting models to $\log_{10}(M_{\text{ej}})$ instead of the M_{ej} . Another reason to use $\log_{10}(M_{\text{ej}})$ is that the error measure adopted for this work, Eq. (2), would otherwise give a strong bias towards data with overall lower values of M_{ej} . An alternative option could be to minimize the residuals; we find that the two approaches provide equivalent results in the domain of calibration of the fits.

Regarding Eq. (9) and Eq. (10), we also note that these formulae deliver ill-conditioned fits, with coefficients that change up to a factor of two for the same data, depending on the guesses or on the nonlinear fitting algorithm employed. Moreover, the compactness in Eq. (10) enters in two additive terms with opposite trends; the physical meaning of this choice is not clear.

Fitting coefficients are reported in Appendix A: coefficients of the polynomial regressions are reported in Tab. IV; fits coefficients for Eqs.(9)-(10) are reported in Tab. V.

The different fits for the dynamical ejecta properties are compared in terms of the reduced χ -squared, χ^2_{ν} , in

Tab. II. Focusing first on **M0RefSet**, we find that for the ejecta mass, M_{ej} , the smallest $\chi^2_{\nu} = 1.55$ comes from fitting the data with the second order polynomial, $P_2^2(q, \tilde{\Lambda})$. A similar result is achieved with Eq. (10), which gives $\chi^2_{\nu} = 1.58$. Adding the models of **M0/M1Set** results in a sharp increase in χ^2_{ν} for all the fitting models. This is due to **M0RefSet** having a narrow span in $\tilde{\Lambda}$, while the additional data have a broader range in $\tilde{\Lambda}$ but similar ejecta masses to the ones reported in **M0RefSet**.

Adding more sets of data with similar extend in the $\tilde{\Lambda}$ parameter does not lead to a significant increase in χ^2_{ν} . If all the datasets are taken into account, the best fit for the ejecta mass is given by Eq. (10), $\chi^2_{\nu} = 39.9$. The second best is $P_2^2(q, \tilde{\Lambda})$, with $\chi^2_{\nu} = 44.4$. The small difference in χ^2_{ν} between these two fitting models can be attributed to the fact that both include the mass ratio explicitly, which allows to capture the leading trend in

TABLE II. Reduced χ -squared χ^2_{ν} for different fitting models for the dynamical ejecta properties. Mean is the simulation average, $P_n(x, y)$ is a polynomial of order n in the variables x, y . Fits are performed for the data of this work and for an increasingly larger combined dataset from the literature. See text for discussion. The best fitting model is characterized by the lowest value of χ^2_{ν} .

$\log_{10}(M_{\text{ej}})$	Datasets	Mean	Eq. (9)	Eq. (10)	$P_2^1(\tilde{\Lambda})$	$P_2^2(q, \tilde{\Lambda})$
	M0RefSet	3.84	2.23	1.58	3.03	1.55
	& M0/M1Set	26.66	16.85	10.60	37.29	56.45
	& LeakSet	99.11	30.12	11.91	45.59	24.40
	& NoNusSet	196.52	84.81	39.88	123.56	44.36
$\langle v_{\text{ej}} \rangle$	Datasets	Mean	Eq. (12)		$P_2^1(\tilde{\Lambda})$	$P_2^2(q, \tilde{\Lambda})$
	M0RefSet	3.76	1.51		3.24	1.05
	& M0/M1Set	4.03	2.42		3.35	1.67
	& LeakSet	7.10	6.07		6.34	5.09
	& NoNusSet	7.95	6.79		7.64	6.83
$\langle Y_{\text{e}} \rangle$	datasets	Mean			$P_2^1(\tilde{\Lambda})$	$P_2^2(q, \tilde{\Lambda})$
	M0RefSet	42.49			43.69	9.07
	& M0/M1Set	37.78			38.62	9.68
	& LeakSet	35.80			36.27	24.96
$\langle \theta_{\text{RMS}} \rangle$	datasets	Mean			$P_2^1(\tilde{\Lambda})$	$P_2^2(q, \tilde{\Lambda})$
	M0RefSet	20.68			21.66	4.55
	& M0/M1Set	18.18			18.69	4.17
	& LeakSet	15.56			14.34	8.73

the data. Also Eq. (9) includes the mass ratio, but it has more coefficients, resulting in more degrees of freedom. In addition, it was previously found in [64], that this fit model does not accurately reproduce the data and misses systematic trends. The simplest model, a polynomial of only $\tilde{\Lambda}$, cannot capture leading trends in the data, resulting in $\chi^2_{\nu} = 123.5$ once all datasets are considered. Similarly, taking the simple mean value as a fitting model results in an even larger $\chi^2_{\nu} = 196.5$. Thus, the inclusion of the dependency on mass-ratio is of crucial importance for modeling dynamical ejecta mass.

In Fig. 2 we show the relative differences between all datasets values and values from the fitting models. We observe that none of the fitting models can adequately

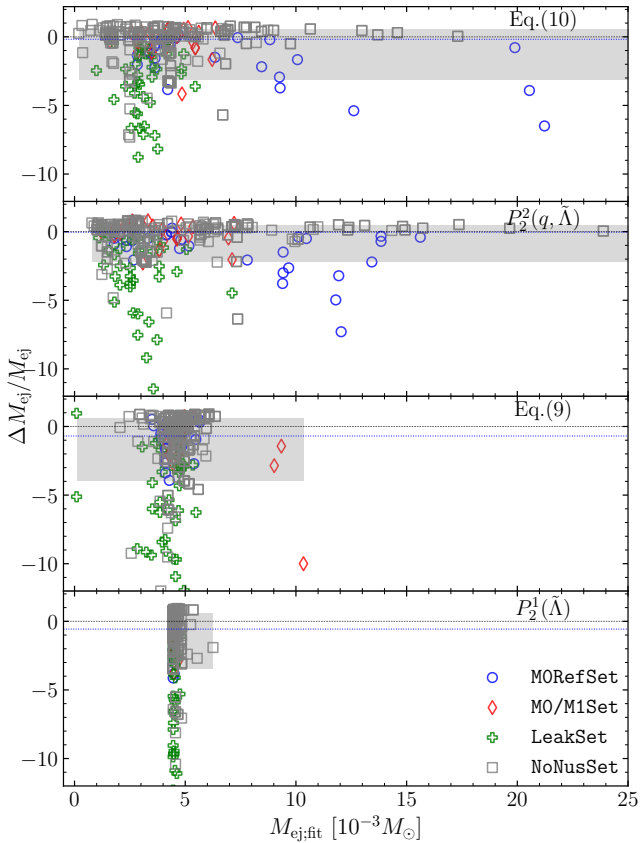


FIG. 2. Relative differences between data and fits for the dynamical ejecta mass, $\Delta M_{\text{ej}} = M_{\text{ej}} - M_{\text{ej}}^{\text{fit}}$. We show polynomial fits and fitting formulae Eq. (9) and Eq. (10). From top to bottom the models arrange based on their χ^2_{ν} : from lowest to highest. The gray region represents the fit's 68% confidence level. Note that while $P_2^2(q, \tilde{\Lambda})$ gives the second lowest χ^2_{ν} the plot shows that it has tighter residuals than the best fit Eq.(10). This is because Eq.(10) fits better models with small M_{ej} , with tighter error bars, Eq. (2). Hence, the χ^2_{ν} is smaller. Note that fitting was performed minimizing $\log_{10}(M_{\text{ej}})$. See text for details.

capture the subset of **LeakSet** with a leakage scheme only as neutrino treatment, (Cf. [63, 64]). While the lowest χ^2_{ν} is found for Eq. (10), the plot shows that the simple polynomial $P_2^2(q, \tilde{\Lambda})$, captures slightly better the high mass tail. Notably Eq. (9) cannot capture that tail, truncating the distribution at $\sim 10^{-2} M_{\odot}$. The polynomial in $\tilde{\Lambda}$ fits the data very poorly, showing an almost flat distribution around the mean value of the ejecta mass.

We conclude that the ejecta mass depends sensibly on the physics included in the simulations and shows various trends in models with polytropic or microphysical EOSs, or when neutrino absorption is taken into account. Across all models the leading trend appears to be given by the mass-ratio. We recommend the use of the $P_2^2(q, \tilde{\Lambda})$ fit with the coefficients given by **M0/M1Set**.

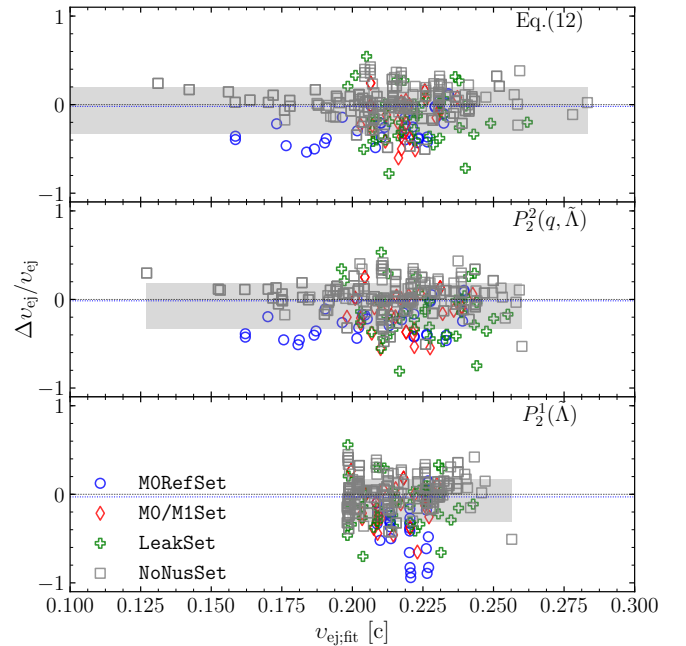


FIG. 3. Relative differences between data and fits for the mass-averaged velocity of the dynamical ejecta, $\Delta v_{\text{ej}} = v_{\text{ej}} - v_{\text{ej}}^{\text{fit}}$. We show the fitting formula Eq. (12) and the polynomial fits. From top to bottom the models are arranged based on their χ^2_{ν} : from lowest to highest.

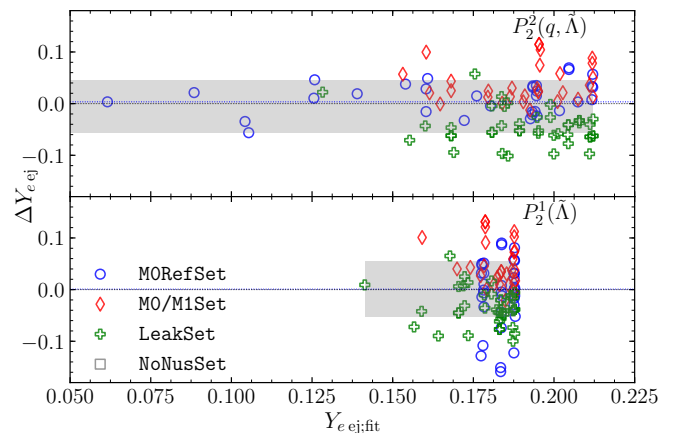


FIG. 4. Relative differences between data and fits for the mass-averaged electron fraction of the dynamical ejecta. We show the polynomial fits, and Eq. (7) and Eq. (IV). Here $\Delta Y_{e, \text{ej}} = Y_{e, \text{ej}} - Y_{e, \text{ej}}^{\text{fit}}$. From top to bottom the models are arranged based on their χ^2_{ν} : from lowest to highest.

B. Mass-averaged velocity

The mass-averaged terminal velocity of the dynamical ejecta, $\langle v_{\infty} \rangle$, from **M0RefSet** ranges from $0.11c$ to $0.27c$, in agreement with the leakage simulations performed with the same code in [64]. However, differently from the analysis of [64], the correlation of the $\langle v_{\infty} \rangle$

with the tidal parameter $\tilde{\Lambda}$ was found in the models of **M0RefSet** [34].

The correlation showed that the lower $\tilde{\Lambda}$, the higher the velocity as a consequence of the fact that the dynamical ejecta in comparable-mass mergers are dominated by the shocked component and that the shock velocity is larger the more compact the binary is. On the contrary, for high mass ratios $q \gtrsim 1.5$, the ejecta are dominated by the tidal component and a larger q leads to a smaller $\langle v_\infty \rangle$ in **M0RefSet**.

The mass-averaged velocity, averaged over the simulations of **M0RefSet**, is:

$$\overline{\langle v_\infty \rangle} = (0.17 \pm 0.04) c. \quad (11)$$

Adding the rest of the **M0/M1Set** models we obtain a similar result, $(0.18 \pm 0.04) c$.

Thus, simulations with similar physics input predict the mean of the ejecta velocity robustly. The inclusion of **LeakSet** models raises the mean value only slightly, to $0.19c$. A more significant increase to $0.23c$ is found if models with polytropic EOS and without neutrinos are added, **NoNusSet**. This is largely due to the dataset of [40] (see Fig. 1).

We fit the data with a second-order polynomials, as in Eq. (7), and also with the fit formula reported in [64, 77]:

$$\langle v_\infty \rangle_{\text{fit}} = \left[\alpha \left(\frac{M_A}{M_B} \right) (1 + \gamma C_A) \right] + (A \leftrightarrow B) + \beta. \quad (12)$$

We note again that this formula delivers ill-conditioned fits. The coefficients of the polynomial regressions for $\langle v_\infty \rangle$ are reported in Tab. IV; fits coefficients for Eq. (12) are reported in Tab. V. The fit models' performance is summarized in Tab. II in terms of χ_ν^2 .

We find that for **M0RefSet** alone, the second order polynomial, $P_2^2(q, \tilde{\Lambda})$, shows the best performance with $\chi_\nu^2 = 1.1$. Additionally, Eq. (12) gives the second best fit with $\chi_\nu^2 = 1.5$. The picture does not change qualitatively when all remaining datasets are added, with the exception of the subset of **NoNusSet** from [40]. When all models of all datasets are considered, the Eq. (12) gives a fit comparable with the $P_2(q, \tilde{\Lambda})$ result.

In Fig. 3 we show the differences between the data and the fits for the considered fitting models. We find that Eq. (12) and the second order polynomial in $(q, \tilde{\Lambda})$ reproduce most of the data within an error of $\sim 50\%$. In both cases, the largest deviations are obtained for models of the **LeakSet**, employing a neutrino leakage scheme. The one parameter polynomial of $\tilde{\Lambda}$ fails to capture the low velocity tail of the distribution and overall gives considerably higher differences between the dataset and the model predicted values of $\langle v_\infty \rangle$.

We conclude that while the inclusion of the mass-ratio, q , and of the reduced tidal parameter, $\tilde{\Lambda}$, into the fitting model allows to capture the leading trends, the ejecta velocity is sensitive to the physics input, in particular, to the effects of neutrino absorption.

C. Electron fraction

The mass-averaged electron fraction, $\langle Y_e \rangle$, in **M0RefSet** varies from 0.03 to 0.27 with a mean value:

$$\overline{\langle Y_e \rangle} = 0.18 \pm 0.07. \quad (13)$$

Including other models from **M0/M1Set** we obtain 0.20 ± 0.06 . The increase in the mean value is largely due to the addition of the datasets with the leakage+M1 scheme of [42, 44], (see Fig. 1). In addition, **M0RefSet** includes models with large q , whose dynamical ejecta are dominated by the cold, low- Y_e , tidal component [38]. The Y_e distribution in other datasets does not go that low as most of their models are equal mass, *e.g.*, [45]. Notably, the mean electron fraction of the **LeakSet** alone is 0.14 ± 0.04 , and once this sample is added to **M0/M1Set** and **M0RefSet**, the mean decreases back to the value found ² in **M0RefSet**, *i.e.* 0.18, with standard deviation remaining at 0.06.

Regarding the fitting functions, we explore the low-order polynomials in $(q, \tilde{\Lambda})$ and in $(\tilde{\Lambda})$ only. The coefficients of polynomial regressions are reported in Tab. IV.

Fitting **M0RefSet** with $P_2^2(q, \tilde{\Lambda})$ results in $\chi_\nu^2 = 9.1$. When the other models of **M0/M1Set** are added, χ_ν^2 rises only slightly to 9.7. This suggests that data from models with similar physics input give the leading trend captured by the fit. The data from the **LeakSet** is statistically different, (different physics setup) and as expected, if we try to include it in our $P_2^2(q, \tilde{\Lambda})$ fit, we obtain a larger $\chi_\nu^2 = 24.9$.

In Fig. 4 we show the performance of the different fitting models for the mass-averaged electron fraction of the ejecta. When all datasets are considered, the second order polynomial manages to reproduce both the low- Y_e tail and high Y_e values for models with advanced neutrino treatment. The accurate computation of the electron fraction clearly requires neutrino absorption to be included into simulation setups. The availability of a larger number of simulations with advanced neutrino transport will undoubtedly improve fitting models.

D. Root mean square half opening angle

In light of the high importance of the ejecta geometry to model electromagnetic counterparts to mergers [31], we also investigate the statistical behavior of the mass-averaged RMS half opening angle of the ejecta across the equatorial plane, θ_{RMS} . Following [64], we define the mass-averaged RMS by assuming axial symmetry and computing:

$$\theta_{\text{RMS}} = \frac{180}{\pi} \left(\frac{\sum m_i \theta_i^2}{\sum m_i} \right)^{1/2}, \quad (14)$$

² Note that [63] does not provide electron fraction.

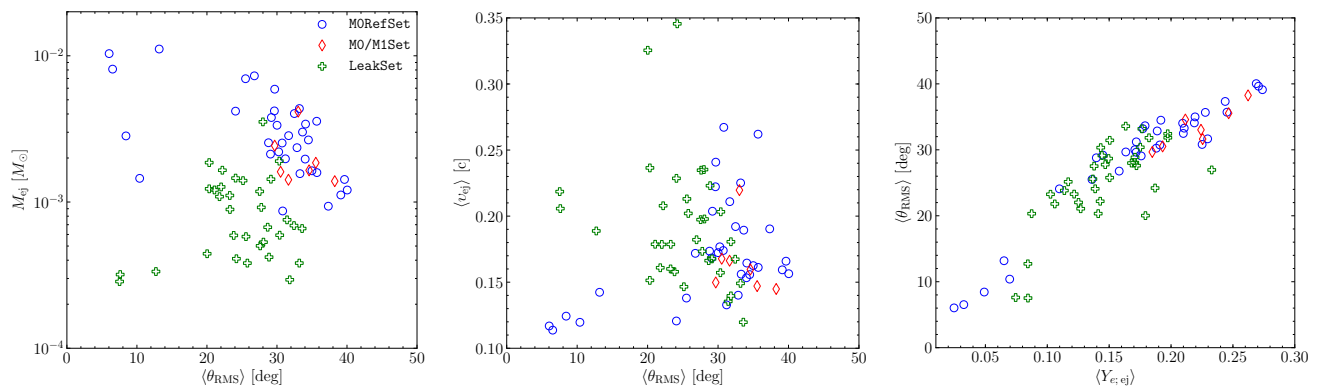


FIG. 5. Relations between the ejecta θ_{RMS} and other parameters of the dynamical ejecta: mass, M_{ej} , velocity, $\langle v_{\infty} \rangle$, and electron fraction $\langle Y_e \rangle$ for models from M0RefSet and [64] from LeakSet and M0/M1Set. Plots show that models with neutrino absorption have higher M_{ej} and larger θ_{RMS} as well as a clear correlation between θ_{RMS} and $\langle Y_e \rangle$.

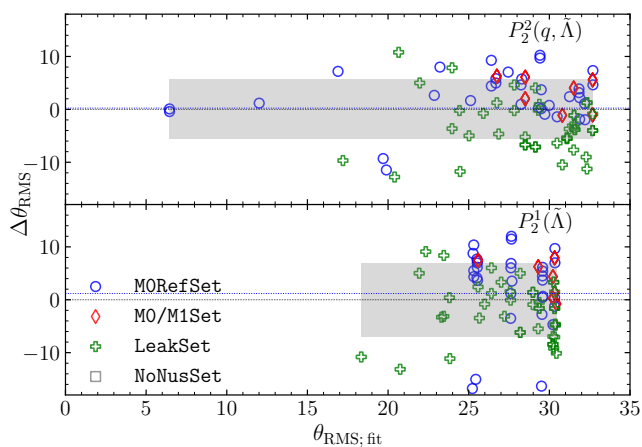


FIG. 6. Relative differences between data and fits of dynamical ejecta mass-averaged electron fraction. We show polynomial fits only. Here $\Delta\theta_{\text{RMS}} = \theta_{\text{RMS}} - \theta_{\text{RMS}}^{\text{fit}}$. From top to bottom the models are arranged based on their χ_{ν}^2 : from lowest to highest.

where θ_i and m_i are the angle (from the binary plane) and mass of the ejecta element. This quantity is available only for M0RefSet and for the models of [64]. In Figure 5 we show the dependency of θ_{RMS} on the previously discussed ejecta parameters. Comparing the data from M0RefSet and the leakage dataset of Ref. [64], we find that the inclusion of neutrino absorption leads to larger θ_{RMS} on average with the exception of highly asymmetric models of M0RefSet. Notably we observe a clear linear relation between the θ_{RMS} and $\langle Y_e \rangle$ (see Fig. 5). The origin of this relation lies in the dependency of the ejecta properties on the binary mass-ratio. Asymmetric binaries produce low- Y_e , tidal ejecta distributed near the plane of the binary, while for more symmetric models with prominent shocked ejecta component there is a tend to have higher Y_e and more spread-out ejecta. The averaged value over

all models of M0RefSet is:

$$\overline{\langle \theta_{\text{RMS}} \rangle} = (28.9 \pm 9.2) \text{ deg}, \quad (15)$$

while together with the dataset of [64] $\overline{\langle \theta_{\text{RMS}} \rangle} = (27.6 \pm 7.9) \text{ deg}$. The decrease in the mean value is due to different physics. In light of the considerably smaller sample of models for which we have θ_{RMS} , we simplify the statistical analysis, considering as fitting models only polynomials: $P_2^2(\tilde{\Lambda})$ and $P_2^2(q, \tilde{\Lambda})$. The coefficients of the polynomial regressions are reported in Tab. IV. Following [64] we adopt a uniform error for all models of 2 degrees. We find that the best fitting model is $P_2^2(q, \tilde{\Lambda})$, which for M0RefSet yields to $\chi_{\nu}^2 = 4.55$. Notably, if we add the M0 models including neutrino absorption of [64](M0), the χ_{ν}^2 decreases to 4.2. However, adding the leakage models of [64](LK) gives $\chi_{\nu}^2 = 8.7$. The comparison between the performance of the different fits in terms of χ_{ν}^2 is presented in Tab. II.

In Fig. 6 we show the performance of polynomial fitting models to the ejecta θ_{RMS} . The second order polynomial provides a better fit to the low- θ_{RMS} tail of the distribution than $P_2^1(\tilde{\Lambda})$. In both cases the error is within $\sim 10 \text{ deg}$. We thus conclude that $P_2^2(q, \tilde{\Lambda})$ is the best fit model to the data. However, the small sample of models does not allow us to conduct a more thorough investigation, in particular, to study the effects of various physics included in simulations.

IV. REMNANT DISK

The disk mass at the end of the simulation of models of M0RefSet varies from $0.01M_{\odot}$ to $0.3M_{\odot}$ with a mean value:

$$\overline{M_{\text{disk}}} = (0.156 \pm 0.084)M_{\odot}. \quad (16)$$

Adding models of M0/M1Set, which are similar with respect to the physical setup, *e.g.*, effects of neutrino ab-

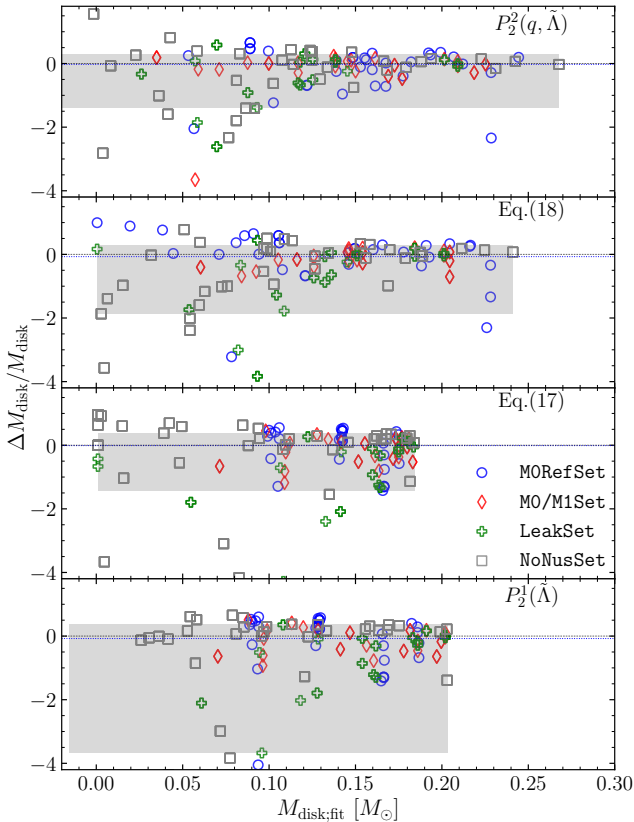


FIG. 7. Relative differences between data and the fits of the disk mass. Different panels show polynomial fits in $\tilde{\Lambda}$ and $(q, \tilde{\Lambda})$, fitting formulae Eq. (9) and Eq. (10). The best fitting model is characterized by the lowest value of χ_ν^2 . Best fitting coefficients are given in the tables in Appendix A. Here $\Delta M_{\text{disk}} = M_{\text{disk}} - M_{\text{disk}}^{\text{fit}}$. The fitting procedure here was based in minimizing residuals instead of χ_ν^2 as otherwise, the error measure adapted, Eq. (3), would lead to the fit underestimating most of datasets used.

TABLE III. Reduced χ -squared χ_ν^2 for different fit models for the final disk mass.

datasets	Mean	Eq. (17)	Eq. (18)	$P_2^1(\tilde{\Lambda})$	$P_2^2(q, \tilde{\Lambda})$
M0RefSet	2956.22	1927.27	2198.85	2574.14	425.41
& M0/M1Set	1523.78	784.72	894.75	1074.14	174.82
& LeakSet	3064.62	543.20	629.95	757.43	202.23
& NoNusSet	2549.50	574.90	442.79	603.87	197.58

sorption and microphysical equation of state. the mean value changes only slightly, $(0.147 \pm 0.075)M_\odot$.

Adding, however, models from the LeakSet results in a decrease of the mean value down to 0.125 with a higher standard deviation of 0.081, as the largest set of models, from Ref. [64], includes low mass binaries that form relatively low mass disks and high mass binaries that form BH at merger with an almost negligible disk left.

Models of the NoNusSet, most of which formed a BH, give disk masses broadly consistent with the other

datasets. While this might suggest that the disk mass depends weakly on the physical setup of simulations, the large uncertainties in data and the fundamental difference between the disk around a neutron star and a black hole must be taken into consideration. In particular, we stress that the disk mass is estimated in different ways in the different datasets. In [60, 77] the disk is estimated only for BNS forming BH, at approximately ≈ 1 ms after collapse and computing the rest mass outside the apparent horizon (AH). In [44], the disk mass is extracted at ≈ 30 ms outside the AH. In [64], the disk mass is computed as the baryonic mass outside the AH at BH formation, while for NS remnants the criterion $\rho < 10^{13}$ g cm^{-3} is used. In [66] for both BH and NS outcome the $\rho < 10^{13}$ g cm^{-3} criterion is used and time of the extraction is not specified. In [45] the density criterion is the same, however the simulations are significantly shorter (~ 7.5 ms) than in other works. Overall, we estimate that these differences can amount to a systematic factor of a few.

We explore the following fitting models: the polynomials, Eqs 7 and , and the formula provided in [64]:

$$\left(\frac{M_{\text{disk}}}{M_\odot}\right)_{\text{fit}} = \max\left\{10^{-3}, \alpha + \beta \tanh\left(\frac{\tilde{\Lambda} - \gamma}{\delta}\right)\right\}, \quad (17)$$

and the fitting formula provided in [70]:

$$\left(\frac{M_{\text{disk}}}{M_\odot}\right)_{\text{fit}} = M_A \max\left\{5 \times 10^{-4}, (\alpha C_A + \beta)^\gamma\right\} + (A \leftrightarrow B). \quad (18)$$

Similarly to the dynamical ejecta mass, the mass of the disk spans up to an order of magnitude, in some cases for very similar values of q and $\tilde{\Lambda}$. However, adopting the approach that was used for the ejecta mass, *i.e.*, considering the $\log_{10}(M_{\text{disk}})$, would result in singularities in certain fits that rely on power-laws and trigonometric functions. Thus, we opt for minimizing the residuals to calibrate the fitting formulae for M_{disk} .

The coefficients of the polynomial regressions are reported in Tab. VI; the fit coefficients for Eq. (17) and Eq. (18) are reported in Tab. VII. The reduced χ^2 for these fits are reported in Tab. IV. As for those for the dynamical ejecta, the formulae in Eq. (17) and Eq. (18) give ill-conditioned fits. Note, in addition, that the fitting function Eq. (18) is not smooth, and can return singular values.

The disk mass M_{disk} depends on both the mass-ratio and $\tilde{\Lambda}$. The statistical analysis shows that indeed the lowest χ_ν^2 is obtained when M0RefSet data are fitted with the second order polynomial in both q and $\tilde{\Lambda}$, giving $\chi_\nu^2 = 425.4$ ³. When the rest of the models of M0/M1Set

³ Note that large values of χ_ν^2 are the result of the fact that fit optimization was performed to minimize the residuals, not the χ_ν^2 . These values should not be compared with χ_ν^2 of ejecta parameters fits.

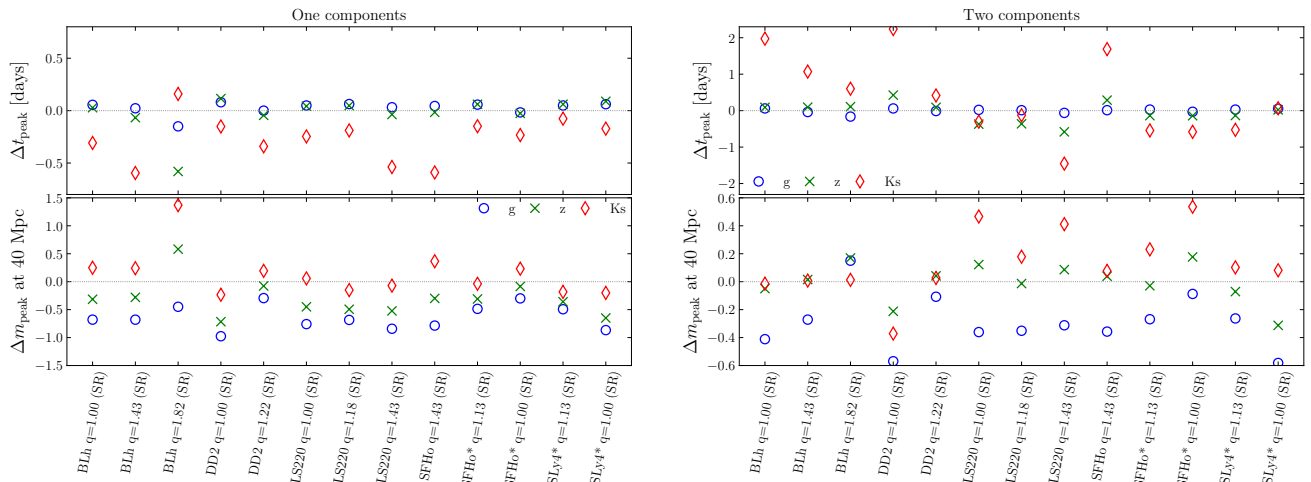


FIG. 8. Comparison between one component light curves (*left panel*) and two components light curves (*right panel*) in g , z and K_s bands using direct NR input or the fitting formulae for the dynamical ejecta and disk mass. The y -axis displays the difference between the peak time (*top panel*), $\Delta t_{\text{peak}} = t_{\text{peak;NR}} - t_{\text{peak;fit}}$, and peak magnitude, $\Delta m_{\text{peak}} = m_{\text{peak;NR}} - m_{\text{peak;fit}}$, (*bottom panel*); the x -axis shows selected BNS models of **MORefSet**. The fits employed here are the polynomials in $(q, \tilde{\Lambda})$ used with the best fitting coefficients, calibrated to **M0/M1Set** (that includes **MORefSet**). The plot shows that the light curves generated with the dynamical ejecta fits (one component) tend to underestimate the peak times and magnitudes of NR-informed light curves, especially in the K_s band. In case of dynamical ejecta and disk wind (two components) light curves, the peak time is less constrained (± 2 days) in the K_s band, but the peak magnitudes is predicted more accurately ± 0.5 mag.

are added, χ^2_{ν} decreases to 174.8, while it rises back to 197.6 when all models are considered. The second best fit model to all datasets is Eq. (18), with $\chi^2_{\nu} = 442.8$.

In Fig. 7 we show the relative differences between the data and the values given by the fitting models. The fitting formulae, Eq. (17) and $P_2^1(\tilde{\Lambda})$, do not predict well the large disk masses observed in high- q runs of **MORefSet**. Eq. (18) performs slightly better in that regard. However, it fails to reproduce values of models from the **NoNusSet**. On the other hand, the use of the polynomial in $(q, \tilde{\Lambda})$ allows to reproduce the high M_{disk} tail and significantly reduces the residuals. This indicates the importance of both tidal deformability and mass-ratio for predicting disk masses of highly asymmetric binaries. Errors in this fitting formulae remain however large, and the disk masses are estimated only within an order of magnitude, given the differences in disk mass extraction methods discussed above.

V. DISCUSSION

In this paper we considered several numerical relativity datasets for the dynamical ejecta properties and the remnant disk mass from binary neutron star mergers. The datasets are computed with different equation of states and neutrino treatment, the latter being the origin of the main differences among the ejecta properties. We compared different fitting models for the ejecta properties and disk mass and find that fitting models based on the reduced tidal parameters and mass ratio can robustly

capture the leading trends in the data. In particular, low order polynomials in these quantities provide a reasonable description of the data available and also favorably compare to the other options in terms of χ^2_{ν} . We advise the use of these polynomial models instead of other fitting formulae proposed in the literature (and also considered in our work) because most of these formulae lead to ill-conditioned fits. Specifically, *our recommendation is to employ Eq. (IV) with the coefficients relative to M0/M1Set (that includes MORefSet) in Tab. IV and Tab. VI and apply these fits to only the region of parameter space that was considered in their calibration* (see Appendix B). We refer to these fits as “best fitting formulae” in our conclusions.

The best fitting formulae studied in this work reproduce rather well the dynamical ejecta velocity (typically to $\sim 50\%$). The electron fraction is reproduced with an accuracy of ~ 0.1 . The ejecta RMS angle about the orbital plane is reproduced with an accuracy of ~ 10 deg. The dynamical ejecta mass, instead is rather uncertain, and can be, at best, reproduced to a factor of a few. Similarly, disk masses are obtained with typical uncertainties of (at least) a factor of a few with the best fitting formulae, although the uncertainties given by different estimation methods only allow to capture the order of magnitude.

The main conclusion of this work is that a statistical analysis with rather simple fitting models clearly displays the uncertainties in the dynamical ejecta computation. In particular, the systematic differences between the datasets due to the EOS models and neutrino treat-

ment in the numerical relativity simulations quantitatively affect the properties of the dynamical ejecta. Neutrino re-absorption appears to be a crucial component for reliable estimates of the dynamical ejecta mass, e.g. [31, 41, 42, 82], and cannot be excluded from future simulations. Simulations of sequences of binaries at different chirp masses could also be useful to identify new trends in the data that cannot be currently explored.

Fitting formulae to the ejecta properties and disk mass are commonly used to study sources of the gravitational waves and electromagnetic counterparts. However, caution ought to be exercised when applying the fitting formulae presented here to infer the source parameters from observations.

As an example, we discuss the impact of using our best fitting formulae for the computation of synthetic kilonova light curves as opposed to the direct numerical relativity input⁴. We use the semianalytic model of Ref. [31] with one or two kilonova components, *i.e.*, the dynamical ejecta and the disk wind. We consider a set of selected BNS models from the MRefSet with 5 different EOS and several mass ratios between $q = 1.00$ and $q = 1.82$. From the best fitting formulae we estimate the dynamical ejecta mass, velocity and angle separating the low opacity polar part and high opacity part about the plane of the binary, using the θ_{RMS} as a separation angle. For the secular ejecta mass we assume it to be 40% of the disk mass, evaluated from the best fitting formula. The opacities, heating rates and extrinsic parameters are kept fixed in the comparison.

The results are collected in Fig. 8, where we show peak times and peak magnitudes for the g , z , and K_s filters. In the one component case (left panels), we find that the peak times are reproduced on average within ~ 0.2 days in the g and z bands, and within ~ 0.5 days in K_s band. The latter is systematically underestimated. The highly asymmetric binary $q = 1.8$ and BLh EOS shows overall the largest deviations. Peak magnitudes in the three bands computed with the fitting formulae differ by ~ 0.5 mag from the NR informed ones, reaching ~ 1 mag in the g band. In the two component case (right panels) the peak times in the K_s band based on the best fitting formulae are more uncertain and amount to ~ 2 days. The peak magnitude show deviations of $\sim \pm 0.5$ mag in z and K_s bands. The reason why the peak magnitudes are more uncertain in the one compo-

nent case lies in the geometrical effects that are inherited in kilonova models from the numerical relativity data, but are not accounted for when using the fits. While the precise details and origin of these differences can be related to the specific light curve model employed here, this example indicates the minimum systematic variation to be expected in the light curve predictions when using the best fitting formulae.

ACKNOWLEDGMENTS

We thank Erika Holmbeck for useful discussions. S.B., B.D. and F.Z. acknowledge support by the EU H2020 under ERC Starting Grant, no. BinGraSp-714626. D.R. acknowledges support from the U.S. Department of Energy, Office of Science, Division of Nuclear Physics under Award Number(s) DE-SC0021177 and from the National Science Foundation under Grant No. PHY-2011725. Data postprocessing was performed on the Virgo ‘‘Tullio’’ server at Torino supported by INFN.

Appendix A: Tables with fitting coefficients

This appendix summarizes all fit coefficients. Dynamical ejecta coefficients can be found in Tab. IV and Tab. V for the polynomials and fitting formulae respectively. Disk coefficients can be found in Tab VI and Tab. VII for the polynomials and fitting formulae respectively. The coefficients of the recommended fitting formulae, as discussed in the conclusion, are highlighted in the tables.

Appendix B: Parameter space for recommended fits

Fitting the ejecta parameters with unconstrained polynomials implies that the validity of the fit is limited to the parameter space of the data used for calibration. In Fig. 9 we display the inferred ejecta and disk mass from the fit in the whole parameter space of the data that we used, *e.g.*, $q \in [1, 1.8]$, $\tilde{\Lambda} \in (250, 1300)$. It is important to note that most of the models are located at low q and moderate $\tilde{\Lambda}$, *i.e.*, in the lower left corner of the parameter space. The upper right corner, however contains no models and the fit is unconstrained there. Indeed, for large q and $\tilde{\Lambda}$ the predicted ejecta masses are above $10^{-1}M_{\odot}$ which might be not supported by future NR simulations.

-
- [1] I. Arcavi *et al.*, *Nature* **551**, 64 (2017), [arXiv:1710.05843 \[astro-ph.HE\]](#).
 [2] D. A. Coulter *et al.*, *Science* (2017), [10.1126/science.aap9811](#), [Science358,1556(2017)], [arXiv:1710.05452](#)

⁴ The ejecta mass, velocity and electron fraction distributions are used to compute the light curve as in Ref. [75]

- [3] M. R. Drout *et al.*, (2017), [10.1126/science.aag0049](#), [arXiv:1710.05443 \[astro-ph.HE\]](#).
 [4] P. A. Evans *et al.*, (2017), [10.1126/science.aap9580](#), [arXiv:1710.05437 \[astro-ph.HE\]](#).
 [5] G. Hallinan *et al.*, (2017), [10.1126/science.aap9855](#), [arXiv:1710.05435 \[astro-ph.HE\]](#).
 [6] M. M. Kasliwal *et al.*, (2017), [10.1126/science.aap9455](#), [arXiv:1710.05436 \[astro-ph.HE\]](#).

TABLE IV. Dynamical ejecta properties: coefficients for polynomial regression of various quantities. Results for both first order and second order polynomials are reported $P_1^2(\tilde{\Lambda})$ and $P_2^2(q, \tilde{\Lambda})$. The recommended calibration for $P_2^2(q, \tilde{\Lambda})$ is highlighted.

Quantity	Datasets	b_0	b_1	b_2	b_3	b_4	b_5	χ_ν^2	R^2
$\log_{10}(M_{\text{ej}})$	MORefSet	-3.69	4.34×10^{-3}	-3.66×10^{-6}				3.0	0.035
	& MO/M1Set	-2.10	-5.84×10^{-4}	8.86×10^{-8}				37.3	0.056
	& LeakSet	-2.85	8.99×10^{-4}	-7.42×10^{-7}				45.6	0.017
	& NoNusSet	-2.35	-1.29×10^{-5}	1.82×10^{-8}				123.6	-0.020
v_∞ [c]	MORefSet	4.63×10^{-1}	-9.58×10^{-4}	7.30×10^{-7}				3.2	0.213
	& MO/M1Set	3.43×10^{-1}	-4.84×10^{-4}	3.25×10^{-7}				3.3	0.211
	& LeakSet	2.77×10^{-1}	-2.38×10^{-4}	1.39×10^{-7}				6.3	0.133
	& NoNusSet	2.50×10^{-1}	-6.71×10^{-5}	2.16×10^{-8}				7.6	0.051
Y_e	MORefSet	3.17×10^{-1}	-5.82×10^{-4}	5.41×10^{-7}				43.7	0.062
	& MO/M1Set	1.99×10^{-1}	-3.08×10^{-5}	4.62×10^{-8}				38.6	0.026
	& LeakSet	1.45×10^{-1}	1.09×10^{-4}	-6.91×10^{-8}				36.3	0.017
$\langle\theta_{\text{RMS}}\rangle$ [deg]	MORefSet	$4.09 \times 10^{+1}$	-5.32×10^{-2}	5.20×10^{-5}				21.7	0.045
	& MO/M1Set	2.55×10^1	3.76×10^{-3}	4.33×10^{-6}				18.7	0.047
	& LeakSet	1.47×10^1	3.37×10^{-2}	-1.79×10^{-5}				14.3	0.115
$\log_{10}(M_{\text{ej}})$	MORefSet	1.04	-3.31	-6.89×10^{-3}	4.19×10^{-1}	5.09×10^{-3}	5.83×10^{-7}	1.6	0.748
	& MO/M1Set	3.35×10^{-2}	-1.44	-6.24×10^{-3}	-1.36×10^{-1}	3.99×10^{-3}	9.03×10^{-7}	56.4	0.192
	& LeakSet	-5.75	3.84	1.19×10^{-3}	-1.02	-5.72×10^{-4}	-4.98×10^{-7}	24.4	0.122
	& NoNusSet	-4.87	3.63	-1.53×10^{-3}	-1.15	1.09×10^{-3}	7.34×10^{-8}	44.4	0.702
v_∞ [c]	MORefSet	7.20×10^{-1}	-2.04×10^{-1}	-1.20×10^{-3}	-4.05×10^{-2}	3.92×10^{-4}	5.20×10^{-7}	1.1	0.769
	& MO/M1Set	6.39×10^{-1}	-1.98×10^{-1}	-8.98×10^{-4}	-3.63×10^{-2}	3.42×10^{-4}	3.26×10^{-7}	1.7	0.626
	& LeakSet	5.67×10^{-1}	-3.26×10^{-1}	-3.58×10^{-4}	5.35×10^{-2}	1.27×10^{-4}	1.25×10^{-7}	5.1	0.324
	& NoNusSet	4.31×10^{-1}	-2.13×10^{-1}	-6.80×10^{-5}	4.61×10^{-2}	3.06×10^{-6}	2.04×10^{-8}	6.8	0.162
Y_e	MORefSet	-3.13×10^{-2}	2.84×10^{-1}	5.89×10^{-4}	-1.48×10^{-1}	-2.02×10^{-4}	-2.78×10^{-7}	9.1	0.824
	& MO/M1Set	2.65×10^{-1}	2.52×10^{-2}	2.31×10^{-4}	-6.28×10^{-2}	-1.88×10^{-4}	-1.86×10^{-8}	9.7	0.768
	& LeakSet	-2.53×10^{-1}	6.26×10^{-1}	5.02×10^{-4}	-2.39×10^{-1}	-3.04×10^{-4}	-1.25×10^{-7}	25.0	0.345
$\langle\theta_{\text{RMS}}\rangle$ [deg]	MORefSet	-6.85×10^1	1.29×10^2	1.18×10^{-1}	$-5.31 \times 10^{+1}$	-2.78×10^{-2}	-6.97×10^{-5}	4.5	0.819
	& MO/M1Set	-4.80×10^1	1.21×10^2	5.92×10^{-2}	$-5.10 \times 10^{+1}$	-2.26×10^{-2}	-2.52×10^{-5}	4.2	0.804
	& LeakSet	-1.04×10^2	1.77×10^2	1.10×10^{-1}	$-6.04 \times 10^{+1}$	-6.50×10^{-2}	-2.47×10^{-5}	8.7	0.483

TABLE V. Dynamical ejecta properties: coefficients for the fitting formulae discussed in the text for various datasets.

Quantity	Fit	Datasets	α	β	γ	δ	n	χ_ν^2	R^2
$\log_{10}(M_{\text{ej}})$	Eq. (9)	MORefSet	1.089×10^{-1}	4.900×10^{-1}	6.487	-7.187	3.110×10^{-1}	2.2	0.401
		& MO/M1Set	-1.172×10^{-1}	-4.157×10^{-1}	2.434×10^{-1}	2.363×10^{-1}	3.175×10^{-1}	16.9	0.079
		& LeakSet	-1.448×10^{-1}	-1.433	2.487	2.827	3.004×10^{-1}	30.1	0.112
		& NoNusSet	1.370×10^{-2}	-6.171×10^{-1}	2.202	-1.279	5.503×10^{-1}	84.8	0.016
$\log_{10}(M_{\text{ej}})$	Eq. (10)	MORefSet	-1.914×10^{-3}	2.204×10^{-2}		-6.912×10^{-2}	1.288	1.6	0.527
		& MO/M1Set	-1.051×10^{-3}	1.160×10^{-2}		-3.717×10^{-2}	1.299	10.6	0.158
		& LeakSet	-1.212×10^{-3}	1.351×10^{-2}		-4.319×10^{-2}	1.318	11.9	0.241
		& NoNusSet	-3.667×10^{-4}	3.100×10^{-3}		-1.068×10^{-2}	1.628	39.9	-0.214
v_∞ [c]	Eq. (12)	MORefSet	-7.591×10^{-1}	1.333	-1.541			1.5	0.635
		& MO/M1Set	-5.867×10^{-01}	1.145	-1.207			2.4	0.428
		& LeakSet	-4.089×10^{-1}	9.296×10^{-1}	-7.041×10^{-1}			6.1	0.170
		& NoNusSet	-3.650×10^{-1}	8.229×10^{-1}	-1.130			6.8	0.157

- [7] M. Nicholl *et al.*, *Astrophys. J.* **848**, L18 (2017), [arXiv:1710.05456 \[astro-ph.HE\]](#).
- [8] S. J. Smartt *et al.*, *Nature* (2017), 10.1038/nature24303, [arXiv:1710.05841 \[astro-ph.HE\]](#).
- [9] M. Soares-Santos *et al.* (DES), *Astrophys. J.* **848**, L16 (2017), [arXiv:1710.05459 \[astro-ph.HE\]](#).
- [10] N. R. Tanvir *et al.*, *Astrophys. J.* **848**, L27 (2017), [arXiv:1710.05455 \[astro-ph.HE\]](#).
- [11] E. Troja *et al.*, *Nature* (2017), 10.1038/nature24290, [arXiv:1710.05433 \[astro-ph.HE\]](#).
- [12] K. P. Mooley, A. T. Deller, O. Gottlieb, E. Nakar, G. Hallinan, S. Bourke, D. A. Frail, A. Horesh, A. Corsi, and K. Hotokezaka, *Nature* **561**, 355 (2018), [arXiv:1806.09693 \[astro-ph.HE\]](#).
- [13] J. J. Ruan, M. Nynka, D. Haggard, V. Kalogera, and P. Evans, *Astrophys. J.* **853**, L4 (2018), [arXiv:1712.02809 \[astro-ph.HE\]](#).
- [14] J. D. Lyman *et al.*, *Nat. Astron.* **2**, 751 (2018), [arXiv:1801.02669 \[astro-ph.HE\]](#).

TABLE VI. Disk mass: coefficients for polynomial regression of various quantities. Results for both first order and second order polynomials are reported $P_2^1(\tilde{\Lambda})$ and $P_2^2(q, \tilde{\Lambda})$. The recommended calibration for $P_2^2(q, \tilde{\Lambda})$ is highlighted.

Datasets	b_0	b_1	b_2	b_3	b_4	b_5	χ^2_ν	R^2
M0RefSet	-2.40×10^{-2}	5.55×10^{-4}	-3.94×10^{-7}				2574.1	0.027
& M0/M1Set	-1.03×10^{-2}	4.07×10^{-4}	-2.23×10^{-7}				1074.1	0.092
& LeakSet	-7.46×10^{-2}	4.99×10^{-4}	-2.41×10^{-7}				757.4	0.299
& NoNusSet	-6.86×10^{-2}	4.80×10^{-4}	-2.12×10^{-7}				603.9	0.408
M0RefSet	-1.57	2.07	9.83×10^{-4}	-6.67×10^{-1}	-2.55×10^{-4}	-4.61×10^{-7}	425.4	0.415
& M0/M1Set	-1.51	2.04	7.71×10^{-4}	-6.45×10^{-1}	-2.74×10^{-4}	-2.52×10^{-7}	174.8	0.542
& LeakSet	-1.47	2.02	6.85×10^{-4}	-6.28×10^{-1}	-3.17×10^{-4}	-1.44×10^{-7}	202.2	0.671
& NoNusSet	-8.57×10^{-1}	1.13	4.22×10^{-4}	-3.74×10^{-1}	3.46×10^{-5}	-2.13×10^{-7}	197.6	0.659

TABLE VII. Disk mass: coefficients for the fitting formulae discussed in the text for various datasets.

Fit	Datasets	α	β	γ	δ	χ^2_{dof}	R^2
Eq. (17)	M0RefSet	1.457×10^{-1}	2.833×10^{-2}	$4.755 \times 10^{+2}$	4.632	1927.3	0.103
	& M0/M1Set	1.349×10^{-1}	3.322×10^{-2}	$4.578 \times 10^{+2}$	1.945×10^{-1}	784.7	0.173
	& LeakSet	-9.829×10^1	9.845×10^1	$-3.158 \times 10^{+2}$	$1.790 \times 10^{+2}$	543.2	0.342
	& NoNusSet	-3.737×10^1	3.756×10^1	$-9.683 \times 10^{+2}$	$4.028 \times 10^{+2}$	574.9	0.436
Eq. (18)	M0RefSet	-1.017	1.006	1.307×10^1		2198.9	0.152
	& M0/M1Set	-1.789	1.045	8.457		894.8	0.233
	& LeakSet	-4.309	8.633×10^{-1}	1.439		629.9	0.400
	& NoNusSet	-4.247	8.384×10^{-1}	1.349		442.8	0.506

- [15] B. P. Abbott *et al.* (Virgo, LIGO Scientific), *Astrophys. J.* **850**, L39 (2017), [arXiv:1710.05836 \[astro-ph.HE\]](#).
- [16] B. P. Abbott *et al.* (Virgo, LIGO Scientific), *Phys. Rev. Lett.* **119**, 141101 (2017), [arXiv:1709.09660 \[gr-qc\]](#).
- [17] B. P. Abbott *et al.* (LIGO Scientific, Virgo), *Phys. Rev. X* **9**, 011001 (2019), [arXiv:1805.11579 \[gr-qc\]](#).
- [18] B. P. Abbott *et al.* (LIGO Scientific, Virgo), (2018), [10.3847/1538-4357/ab0f3d](#), [arXiv:1810.02581 \[gr-qc\]](#).
- [19] J. M. Lattimer and D. N. Schramm, *Astrophys. J. Letters* **192**, L145 (1974).
- [20] E. Symbalisty and D. N. Schramm, *Astrophys. J. Letters* **22**, 143 (1982).
- [21] L.-X. Li and B. Paczynski, *Astrophys. J.* **507**, L59 (1998), [arXiv:astro-ph/9807272 \[astro-ph\]](#).
- [22] S. R. Kulkarni, (2005), [arXiv:astro-ph/0510256 \[astro-ph\]](#).
- [23] S. Rosswog, M. Liebendoerfer, F. Thielemann, M. Davies, W. Benz, *et al.*, *Astron. Astrophys.* **341**, 499 (1999), [arXiv:astro-ph/9811367 \[astro-ph\]](#).
- [24] S. Rosswog, *Astrophys. J.* **634**, L202 (2005), [arXiv:astro-ph/0508138 \[astro-ph\]](#).
- [25] B. Metzger, G. Martinez-Pinedo, S. Darbha, E. Quataert, A. Arcones, *et al.*, *Mon. Not. Roy. Astron. Soc.* **406**, 2650 (2010), [arXiv:1001.5029 \[astro-ph.HE\]](#).
- [26] L. F. Roberts, D. Kasen, W. H. Lee, and E. Ramirez-Ruiz, *Astrophys. J.* **736**, L21 (2011), [arXiv:1104.5504 \[astro-ph.HE\]](#).
- [27] D. Kasen, N. R. Badnell, and J. Barnes, *Astrophys. J.* **774**, 25 (2013), [arXiv:1303.5788 \[astro-ph.HE\]](#).
- [28] P. S. Cowperthwaite *et al.*, *Astrophys. J.* **848**, L17 (2017), [arXiv:1710.05840 \[astro-ph.HE\]](#).
- [29] V. A. Villar *et al.*, *Astrophys. J.* **851**, L21 (2017), [arXiv:1710.11576 \[astro-ph.HE\]](#).
- [30] M. Tanaka *et al.*, *Publ. Astron. Soc. Jap.* (2017), [10.1093/pasj/psx121](#), [arXiv:1710.05850 \[astro-ph.HE\]](#).
- [31] A. Perego, D. Radice, and S. Bernuzzi, *Astrophys. J.* **850**, L37 (2017), [arXiv:1711.03982 \[astro-ph.HE\]](#).
- [32] K. Kawaguchi, M. Shibata, and M. Tanaka, *Astrophys. J.* **865**, L21 (2018), [arXiv:1806.04088 \[astro-ph.HE\]](#).
- [33] S. Fahlman and R. Fernández, *Astrophys. J.* **869**, L3 (2018), [arXiv:1811.08906 \[astro-ph.HE\]](#).
- [34] V. Nedora, S. Bernuzzi, D. Radice, B. Daszuta, A. Endrizzi, A. Perego, A. Prakash, M. Safarzadeh, F. Schianchi, and D. Logoteta, (2020), [arXiv:2008.04333 \[astro-ph.HE\]](#).
- [35] B. D. Metzger, *Living Rev. Rel.* **23**, 1 (2020), [arXiv:1910.01617 \[astro-ph.HE\]](#).
- [36] M. Shibata and K. Hotokezaka, *Ann. Rev. Nucl. Part. Sci.* **69**, 41 (2019), [arXiv:1908.02350 \[astro-ph.HE\]](#).
- [37] D. Radice, S. Bernuzzi, and A. Perego, *Ann. Rev. Nucl. Part. Sci.* **70** (2020), [10.1146/annurev-nucl-013120-114541](#), [arXiv:2002.03863 \[astro-ph.HE\]](#).
- [38] S. Bernuzzi, Invited Review for GERG (2020), [arXiv:2004.06419 \[astro-ph.HE\]](#).
- [39] K. Hotokezaka, K. Kiuchi, K. Kyutoku, T. Muranushi, Y.-i. Sekiguchi, *et al.*, *Phys. Rev.* **D88**, 044026 (2013), [arXiv:1307.5888 \[astro-ph.HE\]](#).
- [40] A. Bauswein, S. Goriely, and H.-T. Janka, *Astrophys. J.* **773**, 78 (2013), [arXiv:1302.6530 \[astro-ph.SR\]](#).
- [41] S. Wanajo, Y. Sekiguchi, N. Nishimura, K. Kiuchi, K. Kyutoku, and M. Shibata, *Astrophys. J.* **789**, L39 (2014), [arXiv:1402.7317 \[astro-ph.SR\]](#).
- [42] Y. Sekiguchi, K. Kiuchi, K. Kyutoku, and M. Shibata, *Phys. Rev.* **D91**, 064059 (2015), [arXiv:1502.06660 \[astro-ph.HE\]](#).
- [43] D. Radice, F. Galeazzi, J. Lippuner, L. F. Roberts, C. D. Ott, and L. Rezzolla, *Mon. Not. Roy. Astron. Soc.* **460**, 3255 (2016), [arXiv:1601.02426 \[astro-ph.HE\]](#).
- [44] Y. Sekiguchi, K. Kiuchi, K. Kyutoku, M. Shibata, and K. Taniguchi, *Phys. Rev.* **D93**, 124046 (2016),

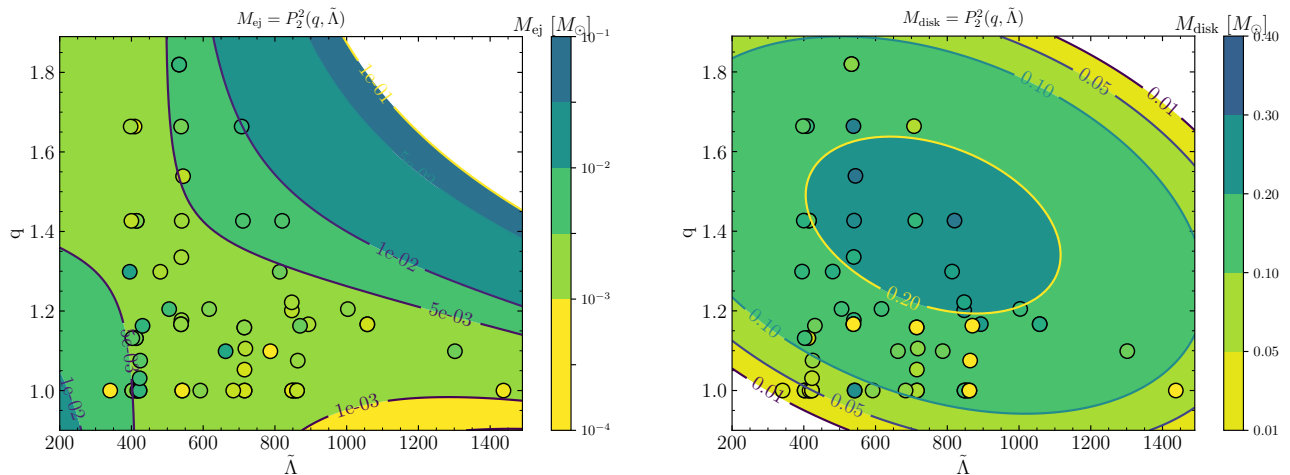


FIG. 9. Ejecta mass (*left panel*) and disk mass (*right panel*) inferred from the $P_2^2(q, \tilde{\lambda})$ fit (colored contours) and ejecta masses from the models of M0RefSet and M0/M1Set, used for its calibration, color-coded. If colors are very close, the fit faithfully reproduces the NR model ejecta mass. Plot shows that within the area of parameter space used for fit formula calibration the ejecta masses of most of the considered models are reproduced. Outside the parameter space, however, the fits should not be used.

- arXiv:1603.01918 [astro-ph.HE].
- [45] T. Vincent, F. Foucart, M. D. Duez, R. Haas, L. E. Kidder, H. P. Pfeiffer, and M. A. Scheel, *Phys. Rev. D* **101**, 044053 (2020), arXiv:1908.00655 [gr-qc].
- [46] L. Dessart, C. Ott, A. Burrows, S. Rosswog, and E. Livne, *Astrophys. J.* **690**, 1681 (2009), arXiv:0806.4380 [astro-ph].
- [47] R. Fernández, E. Quataert, J. Schwab, D. Kasen, and S. Rosswog, *Mon. Not. Roy. Astron. Soc.* **449**, 390 (2015), arXiv:1412.5588 [astro-ph.HE].
- [48] A. Perego, S. Rosswog, R. Cabezon, O. Korobkin, R. Kaeppli, *et al.*, *Mon. Not. Roy. Astron. Soc.* **443**, 3134 (2014), arXiv:1405.6730 [astro-ph.HE].
- [49] O. Just, A. Bauswein, R. A. Pulpillo, S. Goriely, and H. T. Janka, *Mon. Not. Roy. Astron. Soc.* **448**, 541 (2015), arXiv:1406.2687 [astro-ph.SR].
- [50] D. Kasen, R. Fernández, and B. Metzger, *Mon. Not. Roy. Astron. Soc.* **450**, 1777 (2015), arXiv:1411.3726 [astro-ph.HE].
- [51] B. D. Metzger and R. Fernández, *Mon. Not. Roy. Astron. Soc.* **441**, 3444 (2014), arXiv:1402.4803 [astro-ph.HE].
- [52] D. Martin, A. Perego, A. Arcones, F.-K. Thielemann, O. Korobkin, and S. Rosswog, *Astrophys. J.* **813**, 2 (2015), arXiv:1506.05048 [astro-ph.SR].
- [53] M.-R. Wu, R. Fernández, G. Martínez-Pinedo, and B. D. Metzger, *Mon. Not. Roy. Astron. Soc.* **463**, 2323 (2016), arXiv:1607.05290 [astro-ph.HE].
- [54] D. M. Siegel and B. D. Metzger, *Phys. Rev. Lett.* **119**, 231102 (2017), arXiv:1705.05473 [astro-ph.HE].
- [55] S. Fujibayashi, K. Kiuchi, N. Nishimura, Y. Sekiguchi, and M. Shibata, *Astrophys. J.* **860**, 64 (2018), arXiv:1711.02093 [astro-ph.HE].
- [56] B. D. Metzger, T. A. Thompson, and E. Quataert, *Astrophys. J.* **856**, 101 (2018), arXiv:1801.04286 [astro-ph.HE].
- [57] R. Fernández, A. Tchekhovskoy, E. Quataert, F. Foucart, and D. Kasen, *Mon. Not. Roy. Astron. Soc.* **482**, 3373 (2019), arXiv:1808.00461 [astro-ph.HE].
- [58] J. M. Miller, B. R. Ryan, J. C. Dolence, A. Burrows, C. J. Fontes, C. L. Fryer, O. Korobkin, J. Lippuner, M. R. Mumpower, and R. T. Wollaeger, *Phys. Rev. D* **100**, 023008 (2019), arXiv:1905.07477 [astro-ph.HE].
- [59] K. Hotokezaka, K. Kiuchi, K. Kyutoku, H. Okawa, Y.-i. Sekiguchi, *et al.*, *Phys. Rev. D* **87**, 024001 (2013), arXiv:1212.0905 [astro-ph.HE].
- [60] T. Dietrich, S. Bernuzzi, M. Ujevic, and B. Brügmann, *Phys. Rev. D* **91**, 124041 (2015), arXiv:1504.01266 [gr-qc].
- [61] C. Palenzuela, S. L. Liebling, D. Neilsen, L. Lehner, O. L. Caballero, E. O'Connor, and M. Anderson, *Phys. Rev. D* **92**, 044045 (2015), arXiv:1505.01607 [gr-qc].
- [62] S. Bernuzzi, D. Radice, C. D. Ott, L. F. Roberts, P. Moesta, and F. Galeazzi, *Phys. Rev. D* **94**, 024023 (2016), arXiv:1512.06397 [gr-qc].
- [63] L. Lehner, S. L. Liebling, C. Palenzuela, O. L. Caballero, E. O'Connor, M. Anderson, and D. Neilsen, *Class. Quant. Grav.* **33**, 184002 (2016), arXiv:1603.00501 [gr-qc].
- [64] D. Radice, A. Perego, K. Hotokezaka, S. A. Fromm, S. Bernuzzi, and L. F. Roberts, *Astrophys. J.* **869**, 130 (2018), arXiv:1809.11161 [astro-ph.HE].
- [65] A. Perego, S. Bernuzzi, and D. Radice, *Eur. Phys. J. A* **55**, 124 (2019), arXiv:1903.07898 [gr-qc].
- [66] K. Kiuchi, K. Kyutoku, M. Shibata, and K. Taniguchi, *Astrophys. J.* **876**, L31 (2019), arXiv:1903.01466 [astro-ph.HE].
- [67] A. Endrizzi, A. Perego, F. M. Fabbri, L. Branca, D. Radice, S. Bernuzzi, B. Giacomazzo, F. Pederiva, and A. Lovato, *Eur. Phys. J. A* **56**, 15 (2020), arXiv:1908.04952 [astro-ph.HE].
- [68] S. Bernuzzi *et al.*, *Mon. Not. Roy. Astron. Soc.* (2020), 10.1093/mnras/staa1860, arXiv:2003.06015 [astro-ph.HE].
- [69] T. Dietrich and M. Ujevic, *Class. Quant. Grav.* **34**, 105014 (2017), arXiv:1612.03665 [gr-qc].

- [70] C. J. Krüger and F. Foucart, *Phys. Rev. D* **101**, 103002 (2020), [arXiv:2002.07728 \[astro-ph.HE\]](#).
- [71] D. Radice, A. Perego, F. Zappa, and S. Bernuzzi, *Astrophys. J.* **852**, L29 (2018), [arXiv:1711.03647 \[astro-ph.HE\]](#).
- [72] M. W. Coughlin, T. Dietrich, B. Margalit, and B. D. Metzger, *Mon. Not. Roy. Astron. Soc.* **489**, L91 (2019), [arXiv:1812.04803 \[astro-ph.HE\]](#).
- [73] M. W. Coughlin, T. Dietrich, S. Antier, M. Bulla, F. Foucart, K. Hotokezaka, G. Raaijmakers, T. Hinderer, and S. Nissanke, (2019), [10.1093/mnras/stz3457](#), [arXiv:1910.11246 \[astro-ph.HE\]](#).
- [74] M. Bonetti, A. Perego, M. Dotti, and G. Cescutti, *Mon. Not. Roy. Astron. Soc.* **490**, 296 (2019), [arXiv:1905.12016 \[astro-ph.HE\]](#).
- [75] V. Nedora, S. Bernuzzi, D. Radice, A. Perego, A. Endrizzi, and N. Ortiz, *Astrophys. J.* **886**, L30 (2019), [arXiv:1907.04872 \[astro-ph.HE\]](#).
- [76] V. Nedora, F. Schianchi, S. Bernuzzi, D. Radice, B. Daszuta, A. Endrizzi, P. Aviral, A. Perego, and F. Zappa, “Mapping dynamical ejecta and disk masses from numerical relativity simulations of neutron star mergers,” (2020).
- [77] T. Dietrich, M. Ujevic, W. Tichy, S. Bernuzzi, and B. Brügmann, *Phys. Rev.* **D95**, 024029 (2017), [arXiv:1607.06636 \[gr-qc\]](#).
- [78] T. Damour and A. Nagar, *Phys. Rev.* **D80**, 084035 (2009), [arXiv:0906.0096 \[gr-qc\]](#).
- [79] M. Favata, *Phys.Rev.Lett.* **112**, 101101 (2014), [arXiv:1310.8288 \[gr-qc\]](#).
- [80] A. Bauswein, T. Baumgarte, and H. T. Janka, *Phys.Rev.Lett.* **111**, 131101 (2013), [arXiv:1307.5191 \[astro-ph.SR\]](#).
- [81] F. Foucart, E. O’Connor, L. Roberts, L. E. Kidder, H. P. Pfeiffer, and M. A. Scheel, *Phys. Rev.* **D94**, 123016 (2016), [arXiv:1607.07450 \[astro-ph.HE\]](#).
- [82] F. Foucart, M. D. Duez, L. E. Kidder, R. Nguyen, H. P. Pfeiffer, and M. A. Scheel, *Phys. Rev.* **D98**, 063007 (2018), [arXiv:1806.02349 \[astro-ph.HE\]](#).
- [83] D. M. Siegel, *Eur. Phys. J. A* **55**, 203 (2019), [arXiv:1901.09044 \[astro-ph.HE\]](#).
- [84] K. Kawaguchi, K. Kyutoku, M. Shibata, and M. Tanaka, *Astrophys. J.* **825**, 52 (2016), [arXiv:1601.07711 \[astro-ph.HE\]](#).